Coupling of bias-induced crystallographic shear planes with charged domain walls in ferroelectric oxide thin films

Myung-Geun Han, Joseph A. Garlow, Matthieu Bugnet, Simon Divilov, Matthew S. J. Marshall, Lijun Wu, Matthew Dawber, Marivi Fernandez-Serra, Gianluigi A. Botton, Sang-Wook Cheong, Frederick J. Walker, Charles H. Ahn, and Yimei Zhu

Phys. Rev. B **94**, 100101 — Published 2 September 2016

DOI: 10.1103/PhysRevB.94.100101

Coupling of bias-induced crystallographic shear planes with charged domain walls in ferroelectric oxide thin films.

Myung-Geun Han[1], Joseph A. Garlow[1,2], Matthieu Bugnet[3], Simon Divilov[4], Matthew S. J. Marshall[5,6], Lijun Wu[1], Matthew Dawber[4], Marivi Fernandez-Serra[4], Gianluigi A. Botton[3], Sang-Wook Cheong[7], Frederick J. Walker[5,6], Charles H. Ahn[5,6] and Yimei Zhu[1]

[1]Condensed Matter Physics & Materials Science, Brookhaven National Laboratory, Upton, NY, USA 11953

[2]Materials Science & Engineering Department, Stony Brook University, Stony Brook, NY, USA 11794

[3]Department of Materials Science and Engineering, McMaster University, Hamilton, ON, Canada, L8S 4L7

[4]Department of Physics and Astronomy, Stony Brook University, Stony Brook, NY, USA 11794

[5]Department of Applied Physics and Center for Research on Interface Structures and Phenomena, Yale University, New Haven, CT, USA 06520

[6]Department of Mechanical Engineering and Materials Science, Yale University, New Haven, CT, USA 06520

[7]Rutgers Center for Emergent Materials and Department of Physics and Astronomy, Rutgers University, Piscataway, NJ, USA 08854

*Corresponding author: mghan@bnl.gov

Abstract

Polar discontinuity at interfaces plays deterministic roles in charge transport, magnetism, and even superconductivity of functional oxides. To date, most polar discontinuity problems have been explored in hetero-interfaces between two dissimilar materials. Here, we show that charged domain walls (CDWs) in epitaxial thin films of ferroelectric $PbZr_{0.2}Ti_{0.8}O_3$ are strongly coupled to polar interfaces through the formation of ½<101>{*h0l*} type crystallographic shear planes (CSPs). Using atomic resolution imaging and spectroscopy we illustrate that the CSPs consist of both conservative and nonconservative segments when coupled to the CDWs, where necessary compensating charges for stabilizing the CDWs are associated with vacancies at the CSPs. The CDW/CSP coupling yields an atomically narrow domain walls, consisting of a single atomic layer of oxygen. This study shows that the CDW/CSP coupling is a fascinating venue to develop emergent material properties.

A discontinuity in polarization at surfaces/interfaces produces a bound charge that requires compensation *via* long-range Coulomb interactions. This simple electrostatic analysis was originally used as a criterion for surface stability of ionic or partly ionic crystals with a net dipole moment perpendicular to the surface [1,2]. Recently, it has been successfully utilized in polar/nonpolar oxide heterointerfaces such as $LaAlO_3/SrTiO_3$ that shows characteristic two-dimensional electron gases (2DEG) [3,4]. Furthermore, the strong correlation of compensating charges with competing degrees of freedom in charge,

spin, and lattice can lead to emergent phenomena such as ferromagnetism and superconductivity [5,6].

In a similar manner to polar heterointerfaces, polar discontinuities are also present at charged domain walls (CDWs) in ferroelectrics. For example, the 180^o DW in a head-to-head configuration in tetragonal $PbTiO_3$ is charged with twice the spontaneous polarization, as the polarization direction is reversed across the domain wall. Unlike polar heterointerfaces, the DWs divide chemically and structurally homogeneous materials (domains) and thus can be considered as a polar homointerface [7]. The bound charges at polar homointerfaces also require compensating charges for their stabilization. As with 2DEG at the LAO/STO heterointerface, enhanced charge transports are reported for CDWs, indicating charge accumulation [8–11].

Charge compensation may be achieved in various ways including dielectric responses such as displacements of valence electrons and/or ion cores, changes in valence states of metals, and stoichiometry variations [4,12–14]. All these mechanisms essentially "screen" out the bound charges, making the characteristic 1/r decay of electrostatic potential faster. Recently, charged defects, especially associated with nonstoichiometry, are believed to play an important role in providing compensation charges for both polar heterointerface and homointerface [15,16]. The most relevant defects in transition metal oxides are oxygen vacancies that, when fully ionized, donate electrons to transition metal *d* bands and become double positively charged. With increasing concentration of oxygen vacancies, extended defects are experimentally reported in a form of crystallographic shear planes (CSPs) by accumulation of oxygen vacancies in specific planes and then collapsing and shearing the lattice in WO_3 and ReO_3 compounds [17,18]. In perovskites,

formation of ½<101>{*h0l*}-type CSPs has been reported [19]. Here, ½<101> represents the shift vector associated with shearing operation to form shear plane {*h0l*}. The formation of CSPs may lead to a change in stoichiometry if the shift vector has a component perpendicular to the CSP. On the other hand, if the shift vector lies in the CSP, the resulting interface does not reduce the oxygen content and are thus called conservative CSPs. For example, ½<101>(101) CSP is merely an antiphase boundary. However, significant cation and/or oxygen vacancies may be required even for the formation of conservative CSP due to short distances between metal cations in the CSPs [18,19]. This implies CSPs may be electrically charged, providing mobile or bound charges necessary for charge compensation.

Here, we show that CDWs induced by *in-situ* electric biasing in a ferroelectric oxide thin film are strongly coupled to {*h0l*} polar interfaces by formation of ½<101>{*h0l*} type CSPs. By atomic resolution imaging and spectroscopy, we illustrate that CSPs consist of conservative and nonconservative segments when coupled to CDWs. The CDW/CSP coupling yields an atomically narrow DWs, consisting of a single atomic layer of oxygen. This study shows that CDW/CSP coupling can be a fascinating venue to develop and control emergent material behavior.

We focus on epitaxially grown $PbZr_{0.2}Ti_{0.8}O_3$ (PZT) thin films on Nb-doped (001) $SrTiO_3$ (Nb-STO) substrate. TEM samples were fabricated by focused-ion-beam (FIB) for *in situ* electric biasing using commercial TEM holder (Nanofactory Inc.) [20]. Two sections of PZT thin film in a TEM sample were electrically separated by FIB milling, as shown in Fig. 1(a). The section on the left ("unbiased") is in a closed-circuit condition while the section on the right ("biased") is in an open-circuit condition. After making an

electrical contact to the top electrode (FIB-deposited Pt and sputtered Au layers) of the open-circuit section with the piezo-controlled W probe, an *in situ* electric biasing with 10 V DC was applied only to the open-circuit section to induce CDWs. Figs. 1(b) and (c) show the bright-field (BF) TEM images obtained from unbiased and biased sections, respectively. As shown in dark-field (DF) TEM image (Fig. 1(e)), 180^{o} domain walls are only induced in the biased section (P_{down} domain appearing dark while P_{up} bright due to violation of Friedel's law), consistent with our previous report [20]. Interestingly, noticeable defects are also observed in the biased section, but not in the unbiased section (Fig. 1(c)). The defects can be identified with strong diffraction contrast of dark bands, implying a strain field around the defects. Furthermore, these defects densely decorate head-to-head segments of domain walls, as shown in Figs. 2(a) and 2(b), implying strong interactions with the charged domain walls.

Fig. 2(c) shows an atomic resolution high-angle annular dark-field (HAADF) scanning TEM image of a bias-induced defect inside a P_{up} domain. It shows that the split of the Pb columns expands to about 6 – 7 unit cells along the *b*- and *c*-axes. The geometric center appears to be the TiO_2 plane. Near the geometrical center of the defect, the Pb columns are found almost to be in the TiO_2 planes along the *c*-axis, indicating the displacement of Pb columns by about a half unit cell along the *c*-axis. The Pb-column splitting may be explained by formation of an antiphase boundary (APB) with a ½<011>-type shifting vector. Considering the TEM sample thickness of ~ 50 nm in the electron beam path, it can be concluded that an APB about 6 x 6 unit cells in the *ac* plane may be embedded in the P_{up} domain. In order to understand the effects of the embedded APB on local strain and polarization in the matrix P_{up} domain, we measured the displacements of

Ti columns in the orange-boxed area of Fig. 2(c) with respect to the geometric center of Pb lattice and the Pb-Pb distances along the *c*-axis. The Ti displacements with respect to the geometric center of Pb lattice are known to be linearly proportional to the dipole moments [21]. All cation (Pb and Zr/Ti) columns in the P_{up} domain are repelled from the geometric center of the defect, as shown in Fig. 2(d). As a result, the Pb - Pb distances along the *c*-axis are increased both below and above the defect (Fig. 2(e)). However, about five Pb columns surrounding the defect center appear to be almost undistorted, indicating negligible strain at the defect center. Noticeably, the measured Ti displacements (Fig. 2(g)), immediately below the defect center, are a factor of three larger than the bulk value. The Ti displacements below the defect eventually saturate to the bulk value of the Ti displacement with increasing distance from the defect. Meanwhile, the Ti displacements are slightly reduced, or even possibly reversed, above the defect. This asymmetric Ti displacements around the defect suggest that the defect is negatively charged, producing local electric fields pointing towards the defect center along the *c*-axis. Below the defect center, dipole moments are enhanced, because the local electric field is parallel to the polarization. In contrast, above the defect, dipole moments are reduced, as the local electric field is antiparallel.

In Fig. 3(a), DF-TEM image shows bias-induced defects in the segments of CDWs in a head-to-head configuration, as indicated with the arrow heads. In an atomic resolution HAADF STEM image taken from the green-boxed area in Fig. 3(a), the Ti columns are displaced in the opposite directions for P_{up} and P_{down} domains, respectively, as shown in the insets. Along the DWs indicated with the dashed line, there exist significant lattice distortions, consistent with diffraction contrast seen in Figs. 1(c), 2(a),

and 3(a). On the other hand, for neutral domain walls (the inset in the top left corner in Fig. 3(b)) where polarization directions are perpendicular to the domain wall normal, no significant lattice distortions are observed except a ~ 0.7 Å Pb lattice shift, consistent with a previous theoretical study [22].

Three different CSPs with a shift vector ½<101> or ½<111> are observed along the domain wall in Fig. 3(b). Figs. 3(c), 3(d), and 3(e) show the enlarged views of ½[111](001), ½[011](0-11), and ½[-101](101) CSPs, respectively, with corresponding atomic models. ½[011](0-11) and ½[-101](101) CSPs are conservative (APBs) as the shift vectors are in the CSPs. In fact, a clockwise 90^{o} rotation along the *c*-axis transforms the ½[011](0-11) into ½[-101](101) CSP. For the ½[101](101) CSP viewed along the *a*-axis (Fig. 3(e)), both the Pb and Ti columns appear to split (compare the two atomic models shown in Figs. 3(d) and 3(e)) as the P_{up} and P_{down} domains are overlapped in the imaging direction. As a result, the bias-induced defect shown in Fig. 2(c) is a conservative ½[-101](101) CSP, embedded in the P_{up} domain, where the Pb columns are appeared to split as the two antiphases of P_{up} domains are overlapped in the imaging direction. It should be noted that for the ½[-101](101) CSP coupled to CDW in Fig. 3(e), the Pb columns appear to be dimerized along the *c*-axis due to a ~ 0.7 Å shift of Pb lattice between P_{up} and P_{down} domains that are overlapped along the imaging direction. The nonconservative ½[111](001) CSP is similar to the Ruddlesden-Popper phase with a local composition of Pb_2TiO_4 including one TiO_2 missing per unit cell [23]. Strikingly, the Ti displacements are abruptly reversed along the *c*-axis across all three CSPs with atomically sharp domain walls narrower than one unit-cell. Fig. 3(f) shows the measured Ti displacements across the domain wall in Fig. 3(e) with respect to the geometric center

of Pb lattice. The Ti displacements for each column are averaged over 9 unit cells wide. Near the domain wall, the Ti displacements are obtained for both P_{up} and P_{down} domains visible in the three unit cells where the two domains overlap (see the atomic model in Fig. 3(e)). The measured Ti displacements are almost constant in magnitude, even at the domain walls, and abrupt change in their direction is evidenced across the domain wall. Considering the energy cost of abruptly changing dipole moment, this narrowness of DW observed here is remarkable. In contrast, Jia *et al* found that the head-to-head DW in defect-free PZT is approximately 10 unit cell in width [24].

In order to understand charge states at the CDW/CSP, we investigated the Ti valence states, which should be reduced if mobile electrons are accumulated. Figs. 4(a) and 4(b) show Ti-L and O-K edges, respectively, taken from the defect shown in Fig. 3(a) and domain (a few tens nm away from the defect). A noticeable intensity reduction in the e_g and t_{2g} peaks of both the L3 and L2 branch in Ti-L edge are observed when normalized to the post-edges, implying slightly reduced Ti valence states [25]. Considering the Ti columns are mostly Ti^{4+} in the domain as the atomically sharp CSP is tilted from the beam direction (Fig. 3(e)), this reduced valence state is only attributed to the Ti atoms near the CSP. The reduction in the Ti valence state suggests the presence of O vacancies in the system, related with mobile electron accumulation in Ti 3d band near the CSP. The O-K edges in Fig. 4(b) show a slight change in the first peak, as indicated with the arrow (at ~533eV). It is known that the first peak in O-K edge is from the contribution of hybridizations of Ti_{3d} - O_{2p} and Pb_{6p} - O_{2p} [26]. Especially the delayed feature (blue arrow in Fig. 4(b)) that is reduced at the CSP is associated with Pb_{6p}-O_{2p} hybrids, indicating the local decrease in Pb-O bonding. In an atomic model shown in Fig. 4(c), a

formation of ½<101>(101)-type CSP changes the connectivity of octahedral units without altering the coordination number of Ti. Along the CSPs, the octahedra share edges instead of corners, so that the number of oxygen atoms is reduced.

The schematic of an ideal ½<101>(101) CSP/CDW in Fig. 4(c) shows that the geometrical center CDW is an atomic layer of oxygens in the edge-shared octahedral. In addition, it can be clearly seen that the Pb-Pb and Ti-Ti distances at the CSP are about 2.4 Å and 2.6 Å, respectively, much shorter than their standard distances ~ 4 Å in perovskite crystals. These short cation-cation distances are unstable because of their repulsive Coulomb interactions [18]. Abakumov *et al.* reported CS structures in anion-deficient ABO_3 perovskites, suggesting that an additional distortion of 1/3<001> occurs at ½<101>{101} CSPs in order to stabilize the short Pb-Pb distance [27]. The measured Pb-Pb and Ti-Ti distances from the ½[011](0-11) CSP/CDW (Fig. 3(d)) are 3 ± 0.02 Å and 2.8 ± 0.02 Å, respectively, indicating occurrence of additional lattice distortion at the CSPs. The nonbonding lone pair electrons are possibly oriented parallel with the local polarization at the CSP, as shown in Fig. 4(c) [28]. The measured Ti-Ti distance (2.8 ± 0.02 Å) is greater than the value ~2.6 Å for the closest Ti-Ti distance in the corundum structure Ti_2O_3, where two electrons per Ti pair form a direct bond [29], and lower than the value ~2.96 Å for the Ti-Ti distance along the chains of edge-sharing octahedral in rutile TiO_2 [30]. The short metal-metal distances also can be stabilized by formation of significant amounts of A-cation and O-vacancies. The HAADF STEM images in Figs. 3(c) – 3(e) show that intensities of the Pb column become weak at the domain wall, can possibly be linked to the presence Pb vacancies. However, we also note that this weak Pb intensity can be due to a dechanneling effect of the incident electrons associated with

local strain [31]. The exact configuration of Pb/O vacancies and their concentrations, as key information to understand the source of compensating charges of CDW/CSPs, are yet to be determined.

In order to gain insights into charge states associated with vacancies, using first-principle calculations we have calculated the effects of O vacancy, Pb vacancy, and Pb-O divacancy on local dipole moments in both nearest (NN) and next nearest (NNN) neighbor configurations in the $PbTiO_3$ in a supercell consisting of $10x\sqrt{2}x\sqrt{2}$ unit cells, where the stacking occurred along the *c*-axis. We have found that an O (Pb) vacancy induces a tail-to-tail (head-to-head) domain wall in the supercell (see Fig. S1 in Supplementary Material [32]), in agreement with the previous theoretical reports [16,33,34]. For the Pb-O divacancies, we observed in both configurations that the Ti displacements with respect to the Pb lattice are highly asymmetrical along the *c*-axis and increase from their bulk values (see Fig. S2 in Supplementary Material [32]). Especially, NNN configuration provides an abrupt change in Ti displacements. However, it should be noted that a Pb-O divacancy does not produce any mobile electrons or holes as they are charge compensators for each other. Our theoretical study suggests that the head-to-head CDWs shown in Fig. 1 can be stabilized by an accumulation of negatively charged Pb vacancies. However, it should be noted that Pb vacancies act as acceptors and thus cannot induce reduction in Ti valence states. The reduction in Ti valence states found in Fig. 3(a) suggests that there are uncompensated O vacancies in the system. Coulomb interactions would favor the negatively charged Pb vacancies at positively charged DWs, while positively charged O vacancies should be repelled from them. In PZT, it is known that Pb and O vacancies can simultaneously be generated by formation

of volatile PbO gas [35]. It is reported that domain walls act as a gathering site for O vacancies due to local shear strain that reduces formation energy of O vacancies [36]. Chain-like O vacancy clustering on {101} planes has been speculated in $PbTiO_3$ [37] in association with a fatigue mechanism. Taking these factors into account, charge compensation at CDW/CSP may occur as the following. Oxygen vacancies, partially in the form of Pb-O vacancy complexes, are first accumulated on (101) plane, donating electrons for charge compensation by occupying Ti 3d bands near the CDW and then positively charged O vacancies are eliminated by formation of CSPs. It should be noted that FIB-milling and high vacuum (~ 10^{-7} torr) in TEM may affect defect chemistry in PZT samples. However, these effects may not be significant as CSP formations are reported in TEM samples prepared without FIB [27] and electric poling experiment was performed at room temperature without substantial heating. In our *in situ* electric biasing experiment, when the CDWs are coupled to the CSPs, the domain walls are found to be immobile even with external electric fields up to 1 MV/cm, far exceeding the coercive fields (~ 300 kV/cm).

In conclusion, we have found that conservative and nonconservative CSPs are induced in PZT thin films by external biasing in a TEM. These CSPs are electrostatically coupled to the CDWs in head-to-head configuration; negatively charged CSPs effectively compensate the positively charged DWs. The CDW/CSP coupling narrows the width of the domain walls down to a single atomic plane and immobilizes themselves even under external biases exceeding coercive fields.

This work was supported by the Materials Science and Engineering Divisions, Office of Basic Energy Sciences, of the US Department of Energy, under Contract No.

DE-AC02-98CH10886. TEM sample preparation using FIB was performed at the Center for Functional Nanomaterials, Brookhaven National Laboratory. The work at Yale University was supported by NSF MRSEC DMR 119826 (CRISP), DMR 1309868 and FAME. The EELS work was performed at the Canadian Centre for Electron Microscopy, a national facility supported by the Canada Foundation for Innovation through the MSI program, NSERC and McMaster University. The work at Stony Brook University was supported by NSF DMR-1334867. SWC is funded by the Gordon and Betty Moore Foundation's EPiQS Initiative through Grant GBMF4413 to the Rutgers Center for Emergent Materials.

Figure captions

FIG. 1 (a) HAADF STEM image showing the electrical contact made by piezo-controlled W probe. (b) and (c) show BF TEM images showing biased and unbiased sections, respectively. (d) BF (upper) and (e) DF (lower) TEM images from the area indicated with the green box in the (b).

FIG. 2 (a) BF TEM and (b) DF TEM image showing bias-induced defects and positively charged DWs, respectively. (c) HAADF STEM image of a bias-induced defect inside the P_{up} domain. (d) A glancing angle view of (c) showing lattice expansions from the geometrical center, indicated with the white line. (e) Pb-Pb distances measured along the *c*-axis from the orange-boxed area in (c). (f) An arrow map of Ti displacements with respect to local Pb lattice obtained from the orange-boxed area in (c). (g) Line plot of (f) along the *c*-axis showing asymmetric Ti displacements.

FIG. 3 (a) DF TEM showing CSPs (indicated with arrow heads) in the segments of CDWs. The inset highlights DWs (black line) and CSPs (red lines). (b) HAADF STEM image from the area indicated in (a). CSPs coupled with CDWs; 1/2[111](001) (c), 1/2[011](0-11) (d), and 1/2[-101](101) (e). (f) Line profile of Ti displacements measured from (e) along the *c*-axis.

FIG. 4 (a) and (b) Electron energy loss spectra of Ti-L (a) and O-K (b) edges, respectively, taken at a 1/2[101](101) CDW/CSP), as shown in ADF STEM image. (c) Atomic model of an ideal 1/2[-101](101) CDW/CSP.

References

[1] P. W. Tasker, J. Phys. C Solid State Phys. **12**, 4977 (1979).

[2] W. Harrison, E. Kraut, J. Waldrop, and R. Grant, Phys. Rev. B **18**, 4402 (1978).

[3] A. Ohtomo and H. Y. Hwang, Nature **427**, 423 (2004).

[4] N. Nakagawa, H. Y. Hwang, and D. A. Muller, Nat. Mater. **5**, 204 (2006).

[5] J. A. Bert, B. Kalisky, C. Bell, M. Kim, Y. Hikita, H. Y. Hwang, and K. a. Moler, Nat. Phys. **7**, 767 (2011).

[6] N. Reyren, S. Thiel, A. D. Caviglia, L. F. Kourkoutis, G. Hammerl, C. Richter, C. W. Schneider, T. Kopp, A.-S. Ruetschi, D. Jaccard, M. Gabay, D. A. Muller, J.-M. Triscone, and J. Mannhart, Science (80-.). **317**, 1196 (2007).

[7] V. T. Tra, J.-C. Yang, Y.-H. Hsieh, J.-Y. Lin, Y.-C. Chen, and Y.-H. Chu, Phys. Status Solidi – Rapid Res. Lett. **8**, 478 (2014).

[8] J. Seidel, L. W. Martin, Q. He, Q. Zhan, Y.-H. Chu, a Rother, M. E. Hawkridge, P. Maksymovych, P. Yu, M. Gajek, N. Balke, S. V Kalinin, S. Gemming, F.

Wang, G. Catalan, J. F. Scott, N. a Spaldin, J. Orenstein, and R. Ramesh, Nat. Mater. **8**, 229 (2009).

[9] J. Guyonnet, I. Gaponenko, S. Gariglio, and P. Paruch, Adv. Mater. **23**, 5377 (2011).

[10] D. Meier, J. Seidel, a Cano, K. Delaney, Y. Kumagai, M. Mostovoy, N. a Spaldin, R. Ramesh, and M. Fiebig, Nat. Mater. **11**, 284 (2012).

[11] T. Sluka, A. K. Tagantsev, P. Bednyakov, and N. Setter, Nat. Commun. **4**, 1808 (2013).

[12] C. Noguera, J. Phys. Condens. Matter **12**, R367 (2000).

[13] J. Goniakowski, F. Finocchi, and C. Noguera, Reports Prog. Phys. **71**, 016501 (2008).

[14] M. Chisholm, W. Luo, M. Oxley, S. Pantelides, and H. Lee, Phys. Rev. Lett. **105**, 1 (2010).

[15] L. Yu and A. Zunger, Nat. Commun. **5**, 5118 (2014).

[16] C. H. Park and D. J. Chadi, Phys. Rev. B **57**, R13961 (1998).

[17] A. D. Wadsley, Acta Crystallogr. **14**, 664 (1961).

[18] S. Andersson and A. D. Wadsley, Nature **211**, 581 (1966).

[19] C. Bougerol, M. F. Gorius, and I. E. Grey, J. Solid State Chem. **169**, 131 (2002).

[20] M.-G. Han, M. S. J. Marshall, L. Wu, M. a. Schofield, T. Aoki, R. Twesten, J. Hoffman, F. J. Walker, C. H. Ahn, and Y. Zhu, Nat. Commun. **5**, 1 (2014).

[21] C.-L. Jia, V. Nagarajan, J.-Q. He, L. Houben, T. Zhao, R. Ramesh, K. Urban, and R. Waser, Nat. Mater. **6**, 64 (2007).

[22] B. Meyer and D. Vanderbilt, Phys. Rev. B **65**, 1 (2002).

[23] S. N. Ruddlesden and P. Popper, Acta Crystallogr. **10**, 538 (1957).

[24] C.-L. Jia, S.-B. Mi, K. Urban, I. Vrejoiu, M. Alexe, and D. Hesse, Nat. Mater. **7**, 57 (2008).

[25] Y. Shao, C. Maunders, D. Rossouw, T. Kolodiazhnyi, and G. . Botton, Ultramicroscopy **110**, 1014 (2010).

[26] J. C. Jan, H. M. Tsai, C. W. Pao, J. W. Chiou, K. Asokan, K. P. K. Kumar, W. F. Pong, Y. H. Tang, M. H. Tsai, S. Y. Kuo, and W. F. Hsieh, Appl. Phys. Lett. **87**, 87 (2005).

[27] A. M. Abakumov, J. Hadermann, S. Bals, I. V. Nikolaev, E. V. Antipov, and G. Van Tendeloo, Angew. Chem. Int. Ed. Engl. **45**, 6697 (2006).

[28] K. C. Pitike, W. D. Parker, L. Louis, and S. M. Nakhmanson, Phys. Rev. B **91**, 035112 (2015).

[29] B. Y. C. E. Rice and W. R. Robinson, Changes **203**, 1342 (1977).

[30] R. W. G. Wyckoff, *Crystal Structures - Volume 1*, 2nd ed. (Wiley, New York, 1963).

[31] M. Haruta, H. Kurata, H. Komatsu, Y. Shimakawa, and S. Isoda, Ultramicroscopy **109**, 361 (2009).

[32] See Supplemental Material at [URL] for thin film growth conditions, TEM, and DFT calculations.

[33] S. Po□ykko□ and D. J. Chadi, Appl. Phys. Lett. **76**, 499 (2000).

[34] X. Wu and D. Vanderbilt, Phys. Rev. B - Condens. Matter Mater. Phys. **73**, 1 (2006).

[35] R. L. HOLMAN and R. M. FULRATH, J. Am. Ceram. Soc. **55**, 192 (1972).

[36] L. He and D. Vanderbilt, 8 (2003).

[37] J. F. Scott and M. Dawber, Appl. Phys. Lett. **76**, 3801 (2000).

Figure 1.

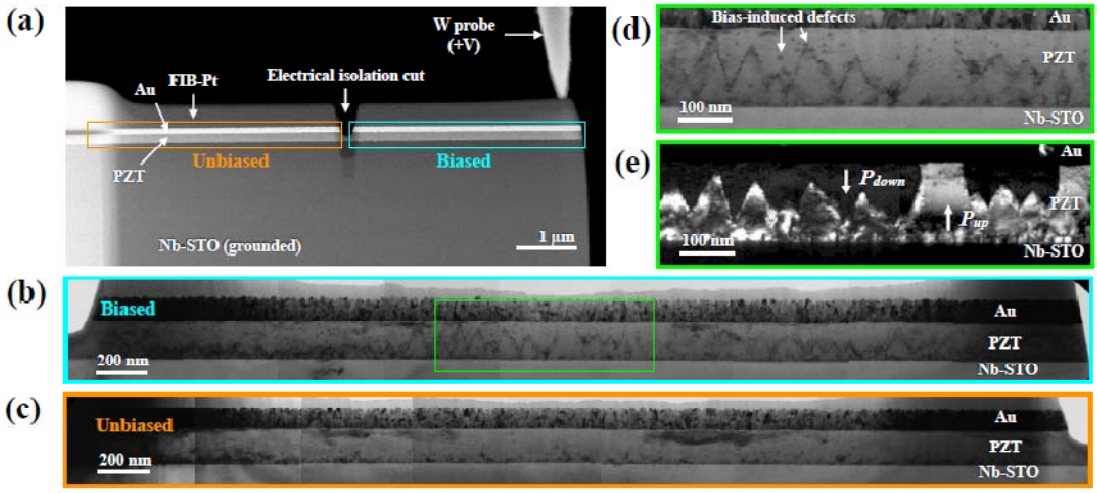
(a)
W probe
(+V)
Au
FIB-Pt
Electrical isolation cut
PZT
Unbiased
Biased
Nb-STO (grounded)
1 μm
(b)
Biased
200 nm
Au
PZT
Nb-STO
(c)
Unbiased
200 nm
Au
PZT
Nb-STO
(d)
Bias-induced defects
Au
PZT
100 nm
Nb-STO
(e)
Au
P_{down}
P_{up}
PZT
100 nm
Nb-STO

Figure 2.

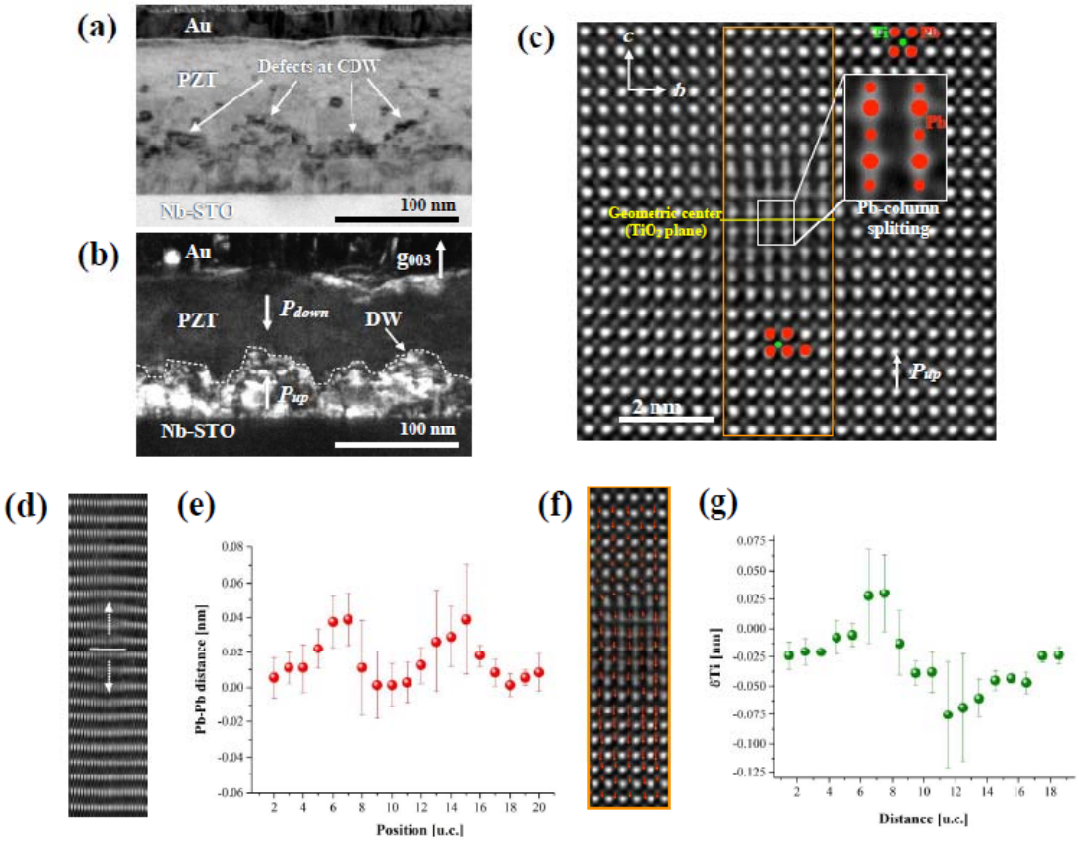
(a)
Au
PZT
Defects at CDW
Nb-STO
100 nm
(b)
Au
g003
PZT
P down
DW
P up
Nb-STO
100 nm
(c)
c
b
Pb
Ti
O
Geometric center (TiO2 plane)
Pb-column splitting
P up
2 nm
(d)
(e)
Pb-Pb distance [nm]
Position [u.c.]
(f)
(g)
δTi [nm]
Distance [u.c.]

Figure 3.

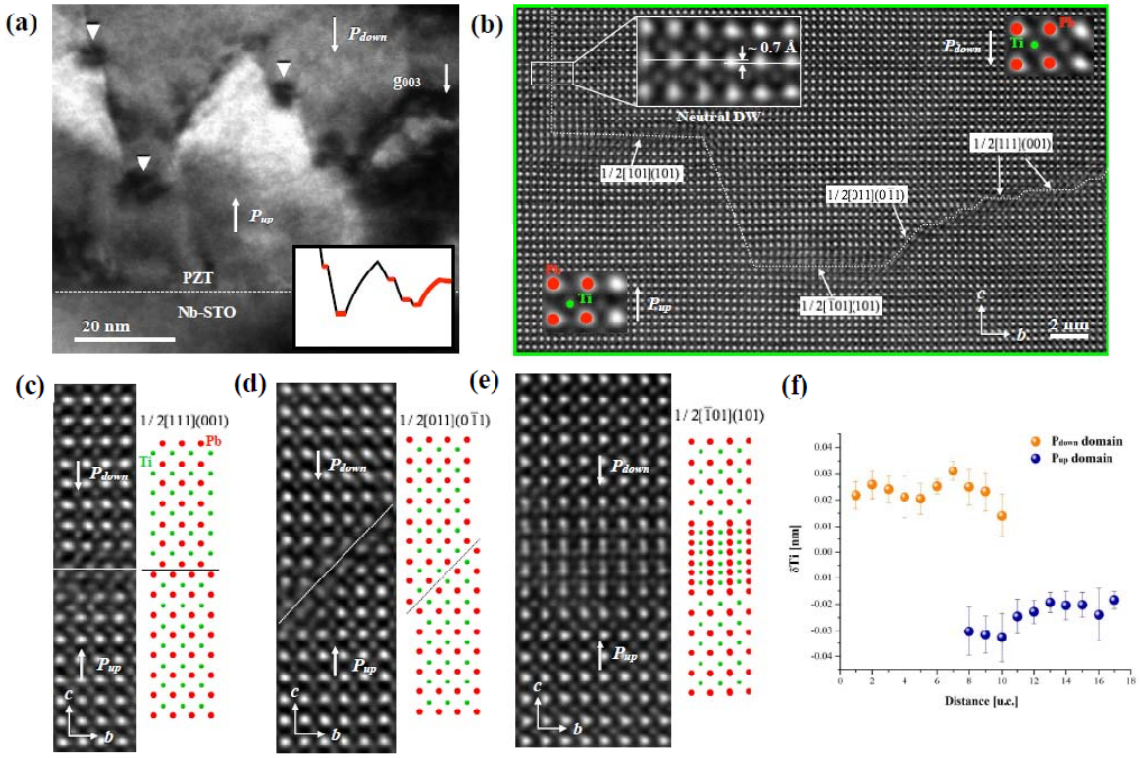
(a)
P_{down}
g_{003}
P_{up}
PZT
Nb-STO
20 nm
(b)
~ 0.7 Å
Neutral DW
P_{down}
Pb
Ti
1/2[101](101)
1/2[111](001)
1/2[011](0$\bar{1}$1)
1/2[$\bar{1}$01](101)
P_{up}
c
b
2 nm
(c)
1/2[111](001)
Pb
Ti
P_{down}
P_{up}
(d)
1/2[011](0$\bar{1}$1)
(e)
1/2[$\bar{1}$01](101)
(f)
P_{down} domain
P_{up} domain
δTi [nm]
Distance [u.c.]

Figure 4.

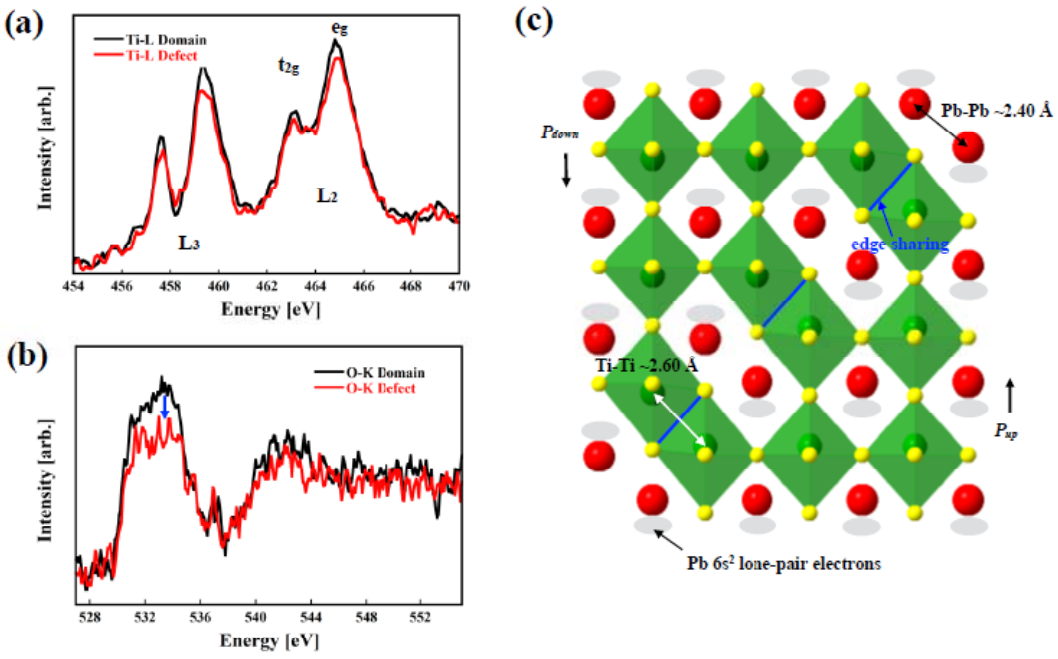
(a)
Ti-L Domain
Ti-L Defect
eg
t2g
L2
L3
Intensity [arb.]
454 456 458 460 462 464 466 468 470
Energy [eV]
(b)
O-K Domain
O-K Defect
Intensity [arb.]
528 532 536 540 544 548 552
Energy [eV]
(c)
Pdown
Pb-Pb ~2.40 Å
edge-sharing
Ti-Ti ~2.60 Å
Pup
Pb 6s2 lone-pair electrons